A98-31495

ICAS-98-2,2,2

Efficiency Improvement of CFD Codes Using Analytical Far-Field Boundary Conditions

A. Verhoff*
The Boeing Company
Saint Louis, Missouri

Abstract

Higher-order far-field computational boundary conditions have been developed for CFD (Computational Fluid Dynamics) calculation of inviscid external flows. They are derived from analytical solutions of an asymptotic form of the steady state Euler equations and have improved accuracy compared to commonly-used characteristic boundary conditions. The analytical solutions provide for a smooth transition across the boundary to the true far-field conditions at infinity. The Euler equations are asymptotically linearized about this constant pressure, rectilinear flow condition. Because the Euler equations are used to develop the boundary conditions, the flow crossing the boundary can be rotational (i.e., applicable to transonic flow calculations). The boundary conditions can be used with any numerical Euler solution method and allow computational boundaries to be located very close to the nonlinear region of interest. This leads to a significant reduction in the number of grid points required for a CFD solution. Because of the proximity of the boundaries, convergence rate of the solution is also increased because fewer iteration steps are required to propagate information between upstream and downstream boundaries. If viscous dissipation is neglected in the far field, the boundary conditions can also be used with Navier-Stokes CFD codes. The procedure also demonstrates the synergism that can be realized from coupling analytical and computational methods.

Introduction

Numerical solution procedures for nonlinear fluid dynamic equations usually use one or more artificial computational boundaries located at some distance from the primary region of interest in order to limit the physical domain to finite size. If the flow crossing such a boundary (either inflow or outflow) is subsonic, then some type of computational boundary conditions must be imposed which simulate the influence of the true far-field conditions at infinity. For steady state external flow problems, these conditions are constant pressure, rectilinear flow.

The computational boundary conditions must be such that waves crossing the boundary do not produce erroneous reflections back into the computational field to degrade the calculations. It is generally acknowledged that it is inappropriate to simply impose free stream conditions (or conditions at infinity) at computational boundaries because of the spurious reflections back into the computational domain which are produced. Standard practice has consisted of locating the boundaries quite far from the region of interest in an attempt to simplify the boundary condition models and minimize any effects of inconsistent modeling. The net effect is a significant increase in the number of grid points required for an accurate flowfield calculation.

Boundary modeling procedures for two-dimensional (2D) internal and external flows were presented in References 1 and 2 which reduce the drawbacks mentioned above and allow the computational boundaries to be located much closer to the nonlinear region of interest. The approach is limited to steady, inviscid flow, although the flow can be rotational. It represents a logical higher-order extension of the so-called characteristic (or zero-order) boundary conditions applied locally which are commonly used with inviscid or viscous numerical solution methods. It also illustrates a consistent procedure for coupling linearized analytical solutions with nonlinear numerical solutions by means of computational boundary conditions. Preliminary extension to three-dimensional (3D) external flow problems was presented in Reference 3.

Use of local zero-order boundary conditions for internal or external flow problems requires that the computational boundaries be located far from the nonlinear near-field region. Close placement of the boundaries may result in a significant amount of solution degradation. The present higher-order procedure is derived from the Euler equations. Therefore, it is applicable to flows which have strong entropy producing effects (e.g., shock waves) within the computational region. Such effects can produce large variations in density and Mach number in the far-field in the direction normal to streamlines (i.e.,

* Boeing Technical Fellow; Assoc. Fellow AIAA

an entropy wake) that persist to infinity and that cannot be treated as small perturbations. A potential flow model (e.g., vortex correction due to lift or some 3D equivalent) of such a far-field having a vorticity wake is inappropriate because its perturbations decay to zero at infinity.

A large number of boundary condition models have been proposed in the literature during the past two decades, and a number of the more prominent works are cited herein (References 4-9). The most noteworthy models are the non-reflecting boundary conditions that strive to suppress erroneous reflections from the boundary back into the computational domain by eliminating all incoming waves. The assumption that nothing occurs beyond the boundary which propagates any meaningful information toward the computational domain is questionable unless the boundary is far removed and incorrect if the flow is rotational. The models are typically derived by linearizing the steady or unsteady fluid dynamic equations (usually Euler) about constant far-field conditions and solving the resulting system assuming a generalized waveform. However, their utility is compromised if strong rotational effects are produced within the computational domain because flow variables other than pressure and flow angle are not constant in the far-field if the flow is treated as inviscid. In that case, linearization in terms of primitive or conservative variables yields perturbation quantities that do not vanish at infinity. Moreover, linearization about average far-field conditions becomes questionable if rotational effects are strong. Streamline-normal gradient variations can be significant, which cause strong interactions to persist in the far-field.

The analysis outlined herein starts from a 3D Euler description in physical space with velocity and flow angles as dependent variables. The equations are rewritten in a linear form derived from the asymptotic far-field behavior wherein pressure is constant and streamlines are rectilinear (true conditions at infinity). The asymptotic analysis allows rotational effects to be taken into account by a change in dependent variable and eliminates the need to linearize the thermodynamic relations. Higher-order compressibility effects that vanish at infinity are treated as right-hand-side (RHS) source terms which are neglected in the far-field asymptotic analysis. These simplified equations are assumed applicable in the far-field region beyond a computational boundary where nonlinear effects are mild.

This development of improved far-field boundary conditions has as its goal the improvement of CFD code efficiency by reducing computational grid size requirements. This is accomplished by allowing artificial boundaries to be placed more proximate where only mild nonlinear effects occur. As was demonstrated in the analysis of Reference 2 for 2D flow, the boundary conditions necessarily depend on the shape of the boundary if they are located where nonlinearities exist. For 2D applications, the boundary shape can be arbitrary while for 3D the analysis is carried out for a computational domain bounded by planar surfaces, as sketched in Figure 1. Construction of a CFD grid which conforms to such an outer boundary shape is not overly restrictive for current grid generation tools, especially unstructured grid methods. The asymptotic form of the Euler equations is solved analytically for the flowfield exterior to the boundary by integral transform techniques.

Coupling of this global analytical solution with the nonlinear numerical (CFD) solution is accomplished by the boundary conditions in an unambiguous manner. The analytical solutions provide a smooth transition across the computational boundary to the true far-field conditions at infinity. The higher-order boundary conditions are in the form of global distributions of flow quantities to be imposed over the boundary, not constant conditions. They represent a logical asymptotic extension of zero-order local conditions for external flows. The additional computational effort required to impose the higher-order boundary conditions is modest. Furthermore, the boundary analysis can be coupled with any inviscid numerical solution method. It can also be coupled with a viscous method by expressing a wake as a vorticity distribution and convecting this distribution downstream via the Euler analytical model, as demonstrated in Reference 10. Viscous dissipation downstream of the boundary is neglected in such an implementation.

Results are presented which establish the validity of the exterior flowfield solutions and boundary conditions. Results using the higher-order boundary conditions are compared with those using zero-order conditions for non-isentropic transonic flows. The CFD code used for the numerical solutions is FL067 (Reference 11). It is demonstrated that the far-field boundaries can be located very close to the body with no loss in accuracy. The reduction in number of grid points required is substantial.

Analytical Formulation

The system of Euler equations asymptotically linearized about a constant pressure far-field state is derived in this section. The formulation is valid for both isentropic and non-isentropic flow conditions.

The three-dimensional form of the steady state Euler equations to be used is

$$(1-M^2)\frac{\partial Q}{\partial x}+\cos\phi\frac{\partial\theta}{\partial y}+\cos^2\theta\frac{\partial\phi}{\partial z}=R_1-\frac{1}{M^2}\frac{\partial S}{\partial x}$$

$$\frac{\partial Q}{\partial y}-\cos\phi\frac{\partial\theta}{\partial x}=R_2-\frac{1}{M^2}\frac{\partial S}{\partial y} \qquad (1)$$

$$\frac{\partial Q}{\partial z}-\frac{\partial\phi}{\partial x}=R_3-\frac{1}{M^2}\frac{\partial S}{\partial z}$$

$$a^2+\frac{\gamma-1}{2}q^2=1 \qquad (2)$$

The RHS terms include higher-order compressibility effects and are defined as

$$R_1\equiv M^2\Big[\sin\theta\cos\theta\cos\phi\frac{\partial Q}{\partial y}+\cos^2\theta\sin\phi\cos\phi\frac{\partial Q}{\partial z}$$
$$-(\sin^2\phi+\sin^2\theta\cos^2\phi)\frac{\partial Q}{\partial x}\Big]-\sin\theta\cos\theta\sin\phi\frac{\partial\phi}{\partial y}$$

$$R_2\equiv M^2\sin\theta\Big[\sin\theta\cos\phi\frac{\partial Q}{\partial x}+\sin\theta\frac{\partial Q}{\partial y}$$
$$+\cos\theta\sin\phi\frac{\partial Q}{\partial z}\Big]+\sin\theta\cos\theta\Big[\sin\phi\frac{\partial\phi}{\partial x}-\cos\phi\frac{\partial\phi}{\partial y}\Big] \qquad (3)$$
$$+\sin\phi\frac{\partial\theta}{\partial z}$$

$$R_3\equiv M^2\cos\theta\sin\phi\Big[\cos\theta\cos\phi\frac{\partial Q}{\partial x}+\cos\theta\sin\phi\frac{\partial Q}{\partial z}$$
$$+\sin\theta\frac{\partial Q}{\partial y}\Big]+\sin\theta\Big[\cos\theta\cos\phi\frac{\partial\phi}{\partial y}-\sin\theta\frac{\partial\phi}{\partial x}\Big]-$$
$$\sin\phi\frac{\partial\theta}{\partial y}$$

Velocity magnitude and speed of sound are denoted by q and a, respectively, and Q is the logarithm of velocity normalized by a reference velocity $\bar{q}_\infty$ defined below. The flow angles θ and ϕ are defined in Figure 2. For two-dimensional flow ϕ is zero. The local Mach number is M and entropy S is defined in terms of pressure p and density ρ as

$$S\equiv\frac{1}{\gamma(\gamma-1)}\ln\left(\frac{p}{\rho^\gamma}\right) \qquad (4)$$

Physical plane Cartesian coordinates are denoted by (x,y,z) and the ratio of specific heats by γ. The fact that entropy remains constant along streamlines has been incorporated into Eqs. (1).

The x-axis can be aligned with the free stream direction without loss of generality. Since θ and ϕ then vanish at infinity, the asymptotic form of Eqs. (1) in the far-field becomes

$$\frac{\partial\theta}{\partial x}-\frac{\partial Q}{\partial y}=\frac{1}{M_\infty^2}\frac{\partial S_\infty}{\partial y}$$
$$\frac{\partial\phi}{\partial x}-\frac{\partial Q}{\partial z}=\frac{1}{M_\infty^2}\frac{\partial S_\infty}{\partial z} \qquad (5)$$
$$\frac{\partial\theta}{\partial y}+\frac{\partial\phi}{\partial z}+(1-M_\infty^2)\frac{\partial Q}{\partial x}=0$$

For non-isentropic flow, M_∞ varies normal to the entropy wake in the downstream far field.

Using the definition (4) and the algebraic total temperature relation (2), the far-field Mach number M_∞ can be expressed as

$$M_\infty^2=\frac{2}{\gamma-1}\frac{1-\bar{a}_\infty^2 e^{(\gamma-1)S_\infty}}{\bar{a}_\infty^2 e^{(\gamma-1)S_\infty}} \qquad (6)$$

The reference speed of sound, velocity, and Mach number are defined as

$$\bar{a}_\infty\equiv p_\infty^{(\gamma-1)/2\gamma}$$
$$\bar{q}_\infty\equiv\sqrt{\frac{2}{\gamma-1}(1-\bar{a}_\infty^2)} \qquad (7)$$
$$\bar{M}_\infty\equiv\bar{q}_\infty/\bar{a}_\infty$$

and are based on the assumption that the far-field pressure p_∞ is constant.

Defining a new dependent variable which includes the far-field entropy by

$$\tilde{Q}\equiv\ln\left\{\sqrt{\frac{\gamma-1}{2}}q\left[1-\bar{a}_\infty^2 e^{(\gamma-1)S_\infty}\right]^{-1/2}\right\} \qquad (8)$$

then Eqs. (5) become

$$\frac{\partial\theta}{\partial x}-\frac{\partial\tilde{Q}}{\partial y}=0$$
$$\frac{\partial\phi}{\partial x}-\frac{\partial\tilde{Q}}{\partial z}=0 \qquad (9)$$
$$\frac{\partial\theta}{\partial y}+\frac{\partial\phi}{\partial z}+\beta^2\frac{\partial\tilde{Q}}{\partial x}=0$$

where

$$\beta^2 \equiv 1 - \overline{M}_\infty^2 \tag{10}$$

Three sets of coordinates are used to develop the far-field solution beyond a planar boundary. Their relationship is shown in Figure 3. The far-field planar grid boundary is coincident with the (Y,Z) plane of the body system (X,Y,Z) related to the computational CFD grid. The X-axis is outwardly normal to the boundary. As stated earlier, the x-axis of the wind system (x,y,z) is parallel with the far-field flow direction, pointing downstream for an outflow boundary and upstream for an inflow boundary. This system is rotated about the x-axis such that the z-axis lies in the (Y,Z) boundary plane. The flow angles θ and ϕ are measured with respect to the wind system as shown in Figure 2. The computational system (ξ,η,ζ) has ξ coincident with X, ζ coincident with z, and η lying in the (x,y) plane. The (η,ζ) plane coincides with the computational boundary plane (Y,Z). The angle between the boundary normal ξ-axis and the x-axis is denoted by ω; ξ is zero on the boundary plane. The angle ω is related to angle of attack and angle of yaw. The computational (analytical) and wind coordinate systems are related by

$$\begin{aligned} \xi &= x\cos\omega - y\sin\omega \\ \eta &= x\sin\omega + y\cos\omega \\ \zeta &= z \end{aligned} \tag{11}$$

These additional coordinate systems are not required for 2D flow, as shown in Reference 2.

In terms of the computational coordinates, the asymptotic equations (9) become

$$\begin{aligned} &\frac{\partial\theta}{\partial\xi} + \tau\frac{\partial\theta}{\partial\eta} - \frac{\partial\tilde{Q}}{\partial\eta} + \tau\frac{\partial\tilde{Q}}{\partial\xi} = 0 \\ &\frac{\partial\phi}{\partial\xi} + \tau\frac{\partial\phi}{\partial\eta} - \frac{1}{\cos\omega}\frac{\partial\tilde{Q}}{\partial\zeta} = 0 \\ &\frac{\partial\theta}{\partial\eta} - \tau\frac{\partial\theta}{\partial\xi} + \frac{1}{\cos\omega}\frac{\partial\phi}{\partial\zeta} + \beta^2\left(\frac{\partial\tilde{Q}}{\partial\xi} + \tau\frac{\partial\tilde{Q}}{\partial\eta}\right) = 0 \end{aligned} \tag{12}$$

where

$$\tau \equiv \tan\omega \tag{13}$$

Further simplification is achieved by the transformation

$$\begin{aligned} &\tilde{\theta} = \theta/\beta \quad \tilde{\phi} = \phi/\beta \\ &u = \xi \qquad v = \beta(\eta - \tau\xi)\cos^2\omega \qquad w = \beta\zeta\cos\omega \end{aligned} \tag{14}$$

which includes a Prandtl-Glauert scaling. Eqs. (12) then become

$$\begin{aligned} &\frac{\partial\tilde{\theta}}{\partial u} - \frac{\partial\tilde{Q}}{\partial v} + \frac{\tau}{\beta}\frac{\partial\tilde{Q}}{\partial u} = 0 \\ &\frac{\partial\tilde{\phi}}{\partial u} - \frac{\partial\tilde{Q}}{\partial w} = 0 \\ &\frac{\partial\tilde{\theta}}{\partial v} - \frac{\tau}{\beta}\frac{\partial\tilde{\theta}}{\partial u} + \frac{\partial\tilde{\phi}}{\partial w} + \frac{\partial\tilde{Q}}{\partial u} = 0 \end{aligned} \tag{15}$$

The boundary plane corresponds to $u = 0$.

Solution Procedure

The homogeneous system (15) provides a higher-order model of the flowfield beyond the computational boundary. The numerical solution inside the boundary propagates information of different type to the inflow and outflow portions of the computational boundary, as described in Reference 12. This differing information serves as boundary conditions for Eqs. (15). The procedure for solution of these equations using Fourier integral transforms is presented in this section. The 2D procedure presented in Reference 2 is somewhat simpler, but follows the same pattern.

The Fourier transformations defined by

$$\begin{aligned} f &\equiv \int_{-\infty}^{\infty} \tilde{Q}\, e^{i\lambda v} dv \quad F \equiv \int_{-\infty}^{\infty} f\, e^{i\mu w} dw \\ g &\equiv \int_{-\infty}^{\infty} \tilde{\theta}\, e^{i\lambda v} dv \quad G \equiv \int_{-\infty}^{\infty} g\, e^{i\mu w} dw \\ h &\equiv \int_{-\infty}^{\infty} \tilde{\phi}\, e^{i\lambda v} dv \quad H \equiv \int_{-\infty}^{\infty} h\, e^{i\mu w} dw \end{aligned} \tag{16}$$

reduces the system (15) to the ordinary differential equations

$$\begin{aligned} &\frac{dG}{du} + i\lambda F + \frac{\tau}{\beta}\frac{dF}{du} = 0 \\ &\frac{dH}{du} + i\mu F = 0 \\ &\frac{dF}{du} - i\lambda G - \frac{\tau}{\beta}\frac{dG}{du} - i\mu H = 0 \end{aligned} \tag{17}$$

The solution of this system is

$$\begin{bmatrix} F \\ G \\ H \end{bmatrix} = C \begin{bmatrix} \lambda\beta\tau - i\beta\sqrt{(\beta^2+\tau^2)\mu^2+\beta^2\lambda^2} \\ \lambda\beta^2 + i\tau\sqrt{(\beta^2+\tau^2)\mu^2+\beta^2\lambda^2} \\ \mu(\beta^2+\tau^2) \end{bmatrix} e^{bu} \qquad (18)$$

where the eigenvalue b is

$$b = -\frac{\beta}{\beta^2+\tau^2}\left[\sqrt{(\beta^2+\tau^2)\mu^2+\beta^2\lambda^2} + i\lambda\tau\right] \qquad (19)$$

and C represents transformed CFD solution boundary values in the computational grid boundary plane. Inversion of the transforms (16) provides the solution for $\tilde{Q}$, $\tilde{\theta}$, and $\tilde{\phi}$.

For the field downstream of an outflow planar boundary, the inversion process gives

$$\tilde{Q} = -\frac{1}{2\pi}\int_{-\infty}^{\infty}\int_{-\infty}^{\infty}\left\{\left[c^2(v-\mu)+\frac{\tau}{\beta}u\right]\tilde{\theta}_b + (w-\sigma)\tilde{\phi}_b\right\}\tilde{G}\,d\mu d\sigma \qquad (20)$$

where the Green's function is defined by

$$\tilde{G} \equiv \left[c^2(v-\mu)^2+(w-\sigma)^2+u^2+2\frac{\tau}{\beta}(v-\mu)u\right]^{-3/2} \qquad (21)$$

and

$$c^2 \equiv \frac{\beta^2+\tau^2}{\beta^2} \qquad (22)$$

The quantities $\tilde{\theta}_b$ and $\tilde{\phi}_b$ represent information propagated to the computational grid boundary by the CFD solution. Likewise, for the field upstream of a planar inflow boundary, the inversion process gives

$$\tilde{\theta} = -\frac{1}{2\pi}\frac{\partial}{\partial v}\int_{-\infty}^{\infty}\int_{-\infty}^{\infty}\frac{\tilde{Q}_b}{(v-\mu)^2+(w-\sigma)^2}\left\{\tilde{G}^{-1/3} - \left[\frac{\tau}{\beta}(v-\mu)u+u^2\right]\tilde{G}^{1/3}\right\}d\mu d\sigma - \frac{\tau}{\beta}\tilde{Q} \qquad (23)$$

$$\tilde{\phi} = -\frac{1}{2\pi}\frac{\partial}{\partial w}\int_{-\infty}^{\infty}\int_{-\infty}^{\infty}\frac{\tilde{Q}_b}{(v-\mu)^2+(w-\sigma)^2}\left\{\tilde{G}^{-1/3} - \left[\frac{\tau}{\beta}(v-\mu)u+u^2\right]\tilde{G}^{1/3}\right\}d\mu d\sigma \qquad (24)$$

The quantity $\tilde{Q}_b$ represents information propagated to the boundary by the CFD solution. This information is typically in the form of the Riemann variable q - 2a/(γ - 1). Using the total temperature relation (2), this quantity can be expressed in terms of boundary velocity q_b, and subsequently Q_b, in a straightforward manner. The quadrature in Eqs. (20), (23) and (24) is performed over the computational boundary surface. The coordinates (μ,σ) lie in the boundary plane.

Development of Boundary Conditions

At a subsonic far-field computational boundary there are four downstream- and one upstream-running wave(s). Therefore, the information available from the numerical solution is not complete and differs at inflow and outflow boundaries. The information lacking must be provided by the boundary conditions. If the flow is supersonic, all waves are downstream-running and specification of boundary conditions is straightforward.

Far-field computational boundary conditions (subsonic) are developed in this section based on the solution of the higher-order Euler model derived in the previous section. This solution is assumed valid in the region beyond the computational boundary where nonlinear effects are not large. Within the computational boundaries the full nonlinear Euler equations must be solved numerically. The boundary conditions provide for a smooth coupling of the nonlinear and far-field solutions so that the true conditions at infinity can be imposed.

The boundary conditions are derived from the analytical solutions (20), (23) and (24) by a limit process wherein u(=ξ) approaches zero. This is an extension of the two-dimensional procedure described in Reference 2. When u=0 the coordinates (v,w) (and (μ,σ)) align with the (η,ζ) coordinates which lie in the (Y,Z) computational grid boundary plane. The quadrature required in the analytical solutions can be carried out by superimposing a rectilinear (v,w) grid on the (Y,Z) plane and interpolating the numerical CFD data onto this grid. Since the computational boundaries are finite (see Figure 1), the numerical information $\tilde{Q}_b$, $\tilde{\theta}_b$ and $\tilde{\phi}_b$ must be extrapolated beyond the edge of the boundaries in order to carry out the quadratures. A low-order polynomial in inverse powers of distance is adequate. The extrapolated regions do not contribute significantly to the overall integration result since $\tilde{Q}_b$, $\tilde{\theta}_b$ and $\tilde{\phi}_b$ are relatively small beyond the edges of

the boundary. This approach was used successfully in Reference 10 for two-dimensional flows.

Inflow Boundary

Along the inflow portion of the boundary (isentropic conditions assumed), there are three downstream-running waves propagating information to the boundary from outside the computational domain (i.e., from upstream infinity) and one upstream-running wave propagating information from the numerical CFD solution (see Reference 12). The incoming information is represented by the Riemann variable $q + 2a/(\gamma - 1)$ and the flow angles θ and ϕ. The outgoing information is represented by the Riemann variable $q - 2a/(\gamma - 1)$. The solutions (23) and (24) provide two of the lacking information elements from outside the computational domain; the remaining information is provided by the total temperature relation (2).

The numerical solution propagates the Riemann variable $q - 2a/(\gamma - 1)$ to the boundary which can be converted to q_b (and Q_b) as explained earlier. Using the total temperature relation the boundary distribution of the downstream propagating Riemann variable (i.e., the boundary conditions) is calculated according to

$$\left(q+\frac{2}{\gamma-1}a\right)_{bc} = q_b + \frac{2}{\gamma-1}\sqrt{1-\frac{\gamma-1}{2}q_b^2} \tag{25}$$

The distribution of flow angles on the inflow portion of the computational boundary is provided by the solutions (23) and (24) as

$$\tilde{\theta}_{bc} = -\frac{1}{2\pi}\frac{\partial}{\partial v}\lim_{u\to o}\int_{-\infty}^{\infty}\int_{-\infty}^{\infty}\frac{\tilde{Q}_b}{(v-\mu)^2+(w-\sigma)^2}\cdot \left[\tilde{G}^{-1/3}-\frac{\tau}{\beta}(v-\mu)u\tilde{G}^{1/3}\right]d\mu d\sigma - \frac{\tau}{\beta}\tilde{Q}_b \tag{26}$$

$$\tilde{\phi}_{bc} = -\frac{1}{2\pi}\frac{\partial}{\partial w}\lim_{u\to o}\int_{-\infty}^{\infty}\int_{-\infty}^{\infty}\frac{\tilde{Q}_b}{(v-\mu)^2+(w-\sigma)^2}\cdot \left[\tilde{G}^{-1/3}-\frac{\tau}{\beta}(v-\mu)u\tilde{G}^{1/3}\right]d\mu d\sigma \tag{27}$$

Within the integrals $\tilde{Q}_b$ represents velocity information propagated to the inflow boundary by the numerical solution, as explained above. This information provides the boundary data for the upstream analytical model. The singularities in the Green's function $\tilde{G}$ are integrable. They can be removed by using an appropriate approximation (e.g., bilinear) for $\tilde{Q}_b$ over individual rectilinear cells with subsequent integration by parts.

Zero-order (or characteristic) boundary conditions would consist of imposing the constant values $\bar{q}_\infty + 2\bar{a}_\infty/(\gamma-1)$, θ = constant, and ϕ = constant along the inflow portion of the boundary.

Outflow Boundary

Along the outflow portion of the boundary there are four (three for isentropic conditions) downstream-running waves propagating information to the boundary from the numerical solution and one upstream-running wave propagating information from outside the computational domain (i.e., from downstream infinity). The solution (20) provides the lacking information from outside the computational domain.

In the limit as u approaches zero, the solution (20) may be written

$$\tilde{Q} = -\frac{1}{2\pi}\lim_{u\to o}\int_{-\infty}^{\infty}\int_{-\infty}^{\infty}\left\{[c^2(v-\mu) + \frac{\tau}{\beta}u]\tilde{\theta}_b + (w-\sigma)\tilde{\phi}_b\right\}\tilde{G}\,d\mu d\sigma \tag{28}$$

The quantities $\tilde{\theta}_b$ and $\tilde{\phi}_b$ represent numerical CFD solution information propagated to the outflow portion of the boundary and provide the boundary data for the downstream analytical model. A suitable approximation for $\tilde{\theta}_b$ and $\tilde{\phi}_b$ over rectilinear cells allows integration by parts and removal of the Green's function singularities.

From the definition (8) the velocity distribution along the outflow portion of the boundary obtained from the analytical solution is

$$q = \sqrt{\frac{2}{\gamma-1}\left[1-\bar{a}_\infty^2 e^{(\gamma-1)S_\infty}\right]}^{1/2} e^{\tilde{Q}} \tag{29}$$

where $\tilde{Q}$ is obtained by quadrature from the relation (28). The quantity S_∞ can be approximated by numerical solution values of S at the boundary for non-isentropic conditions. This approximation neglects streamline curvature downstream of the boundary. Using the total temperature relation (2), the boundary distribution of the upstream propagating Riemann variable (i.e., the boundary conditions) is calculated according to

$$\left(q-\frac{2}{\gamma-1}a\right)_{bc}=\left(q+\frac{2}{\gamma-1}a\right)_{num}-\frac{4}{\gamma-1}\sqrt{1-\frac{\gamma-1}{2}q^2} \quad (30)$$

The value of q under the radical is obtained from Eq. (29) and the remaining RHS term represents information propagated to the boundary by the numerical solution. This formulation uses the analytical solution to describe the pressure field exterior to the outflow boundary.

Conventional practice using zero-order boundary conditions would consist of imposing the constant value $\bar{q}_\infty - 2\bar{a}_\infty/(\gamma-1)$ along the outflow portion of the boundary.

Results

The boundary condition procedures developed above have been implemented in the CFD code FLO67 (Reference 11). Results are presented in this section which compare the higher-order boundary conditions with the commonly-used zero-order conditions. Calculations are presented on grids where the boundaries are very close to an airfoil (2D application) and a wing (3D application). The boundaries are approximately one characteristic length away from the bodies. Accuracy is assessed by comparing with a large-grid baseline solution.

Typical results for 2D application of the higher-order boundary conditions are presented in Figures 4-9. Baseline results for the NACA 0012 airfoil were calculated using FL067 on a large C-grid whose far-field boundary was located approximately 40 chord lengths from the airfoil. This distance was sufficiently large that the zero-order (characteristic) and higher-order boundary conditions produced almost identical results. The calculations were repeated on a much smaller C-grid using both the zero-order and higher-order boundary conditions. The small grid boundaries were very close to the airfoil (approximately one chord). These small grid results are compared with the baseline results from the large grid in order to assess the higher-order boundary condition accuracy.

The small core grid shown in Figure 4 had 241 points in the circumferential direction and 41 points in the radial direction. It extended one chord length upstream of the airfoil leading edge and one chord length downstream of the trailing edge. There were 177 points on the airfoil surface. The large baseline grid had dimensions 305 x 73 and was constructed by simply adding C-lines outside the core grid inflow boundary and vertical lines downstream of the outflow boundary. It extended approximately 40 chord lengths upstream and downstream of the airfoil. The relative locations of the outer boundaries of the two grids are shown in Figure 5.

Transonic surface pressures predicted by the FL067 code using the core grid of Figure 4 are presented in Figure 6. The free stream Mach number was 0.80 and the angle of attack was 2 degrees. Results for both zero-order and higher-order global boundary conditions are shown along with baseline results from the large grid. The higher-order boundary conditions produced results nearly identical to the baseline results, while the zero-order boundary conditions produced considerable solution degradation. The most noticeable effect of the zero-order boundary conditions is the incorrect prediction of the shock location and strength. Pressure contours are shown in Figures 7 and 8. Similar results are obtained for O-grid topologies (see Reference 2).

Overall consistency of the global boundary condition procedure is demonstrated by the transonic Mach number contours shown in Figure 9. Near-field contours from the FLO67 computation on the small O-grid match smoothly with the far-field contours from the analytical solution, including the non-isentropic portion of the field. The computational boundary shape was elliptic to simplify the calculation of the far-field analytical solution and its contours. The boundary was situated approximately one chord length above the airfoil to lie outside of the embedded supersonic region on the upper surface.

The wing used for the 3D calculations had constant chord NACA 0012 airfoil sections and an aspect ratio of 5.2. A large baseline C-grid was constructed about the wing whose outer boundary extended about 40 chord lengths upstream, downstream and vertically. It extended approximately 5 span lengths from the tip in the lateral direction. The baseline grid had dimensions (257x65x25). Results from this baseline grid were used to assess the accuracy of the higher-order boundary condition model when applied to a smaller grid.

The small grid boundaries extended approximately 2 chord lengths upstream and downstream of the wing. The small grid had dimensions (193x41x25) and was coincident with the inner portion of the baseline grid. The boundaries of the small grid were planar, as indicated in Figure 1.

Transonic surface pressures predicted by the FLO67 code using the small grid are shown in Figure 10. The free stream Mach number was 0.70 and the angle of attack was 5 degrees. Pressure coefficients are shown on the center-plane and at 52 percent semi-span. Results for both zero-order and higher-order boundary conditions are compared along with baseline results from the large grid. The higher-order boundary conditions produced results nearly identical to the baseline results, while the zero-order boundary conditions produced typical solution degradation, primarily in the vicinity of the shock wave. Pressure contours at 52 percent semi-span, are shown in Figures 11. Pressure contours at 95 percent semi-span are shown in Figure 12 for a free stream Mach number of 0.40 and an angle of attack of 8 degrees.

Large efficiency gains can be achieved by incorporating more accurate far-field boundary conditions into numerical flowfield solution methods. The number of computational grid points for a given accuracy level can be reduced typically by a factor of 2 by using higher-order conditions. Only a modest increase (approximately 2 percent) in computational effort is required for the higher-order conditions. An additional efficiency gain is also provided in that fewer iterations are typically required for solution convergence because of the closer proximity of the far-field boundaries.

Summary

Far-field computational boundary conditions have been developed for 2D and 3D external flow problems. These higher-order boundary conditions are derived from analytical solutions of an asymptotic form of the Euler equations and represent a logical extension of the zero-order (or characteristic) boundary conditions commonly used in the numerical solution of nonlinear fluid dynamic equations. Transformations are introduced which lead to linear equations to be solved in the far field, but the fluid dynamic variables are not linearized and small perturbations are not assumed. Asymptotic vorticity effects are incorporated into the dependent variable velocity function making the analysis valid for rotational flow. The equations are solved using integral transform techniques giving an analytical description of the flowfield beyond the CFD computational boundaries.

The boundary conditions and analytical solutions provide a smooth transition across a computational boundary to the true far-field conditions at infinity. The boundary procedure is general in that it can be used in conjunction with any inviscid numerical solution method. Because the boundary conditions are derived from the Euler equations, the flow crossing the boundaries can be rotational (non-isentropic) and they can be used for calculating transonic flows containing shock waves. The higher-order global boundary conditions allow the far-field boundaries to be located much closer thereby reducing the number of grid points needed for the numerical solution and also the number of iterations for solution convergence. This allows a significant reduction in the amount of computational effort (i.e., increased efficiency) required for the nonlinear numerical solution because the additional calculations required for the higher-order boundary conditions is modest.

Representing the vorticity distribution of a viscous wake as an entropy distribution and allowing this wake to convect downstream undamped allows the boundary conditions procedure to be used with Navier-Stokes codes for viscous calculations. This viscous flow application is only an approximation, since the Euler analytical far-field model preserves a vorticity wake to infinity, whereas a viscous wake eventually decays.

Acknowledgments

This research was partially supported by the McDonnell Douglas Independent Research and Development Program and partially by the U.S. Air Force under contract F33615-94-C-3000 (Dr. Don W. Kinsey, Program Manager). The author would like to thank Mr. Michael McDevitt for his assistance in carrying out the calculations.

References

1. Verhoff, A., and Stookesberry, D., "Second-Order, Far-Field Computational Boundary Conditions for Inviscid Duct Flow Problems," AIAA Journal, Vol. 30, May 1992, pp. 1268-1276.

2. Verhoff, A., "Global Far-Field Computational Boundary Conditions for C- and O-Grid Topologies," AIAA Journal, Vol. 36, No. 2, February 1998, pp. 148-156.

3. Verhoff, A., "Far-Field Computational Boundary Conditions for Three-Dimensional External Flow Problems," AIAA Paper No. 96-0892, January 1996.

4. Engquist, B., and Majda, A., "Absorbing Boundary Conditions for the Numerical Simulation of Waves," Mathematics of Computation, Vol. 31, No. 139, 1977, pp. 629-651.

5. Higdon, R. L., "Initial-Boundary Value Problems for Linear Hyperbolic Systems," SIAM Review, Vol. 28, No. 2, 1986, pp. 177-217.

6. Giles, M. B., "Nonreflecting Boundary Conditions for Euler Equation Calculations," AIAA Journal, Vol. 28, December 1990, pp. 2050-2058.

7. Hirsch, C., and Verhoff. A., "Far-Field Numerical Boundary Conditions for Internal and Cascade Flow Computations," AIAA Paper No. 89-1943, June 1989.

8. Ferm, L., "Open Boundary Conditions for Stationary Inviscid Flow Problems," Journal of Computational Physics, Vol. 78, No. 1, September 1988, pp. 94-113.

9. Ferm, L., "Open Boundary Conditions for External Flow Problems," Journal of Computational Physics, Vol. 91, No. 1, November 1990, pp. 55-70.

10. Verhoff, A., Stookesberry, D., and Agrawal S., "Far-Field Computational Boundary Conditions for Transonic Flows," 4th International Symposium on Computational Fluid Dynamics, Davis, CA, September 9-12, 1991.

11. Jameson, A., "A Vertex Based Multigrid Algorithm for Three-Dimensional Flow Calculations," ASME AMD, Vol. 78, American Society of Mechanical Engineers, New York, December 1986, pp. 45-73.

12. Verhoff, A., and O'Neil, P. J., "A Natural Formulation for Numerical Solution of the Euler Equations," AIAA Paper No. 84-0163, January 1984.

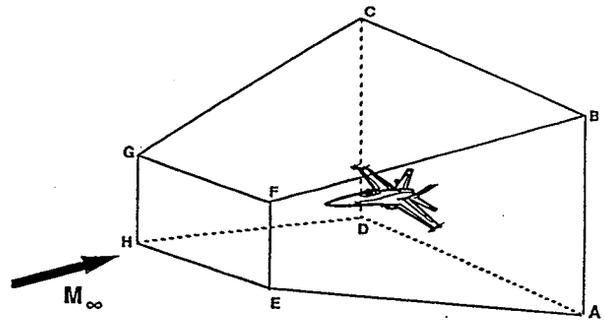

Fig. 1 Computational Domain With Planar Boundaries.

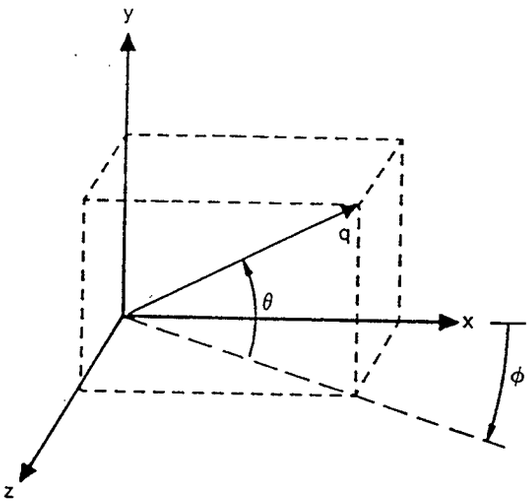

Fig. 2 Flow Angle Definition.

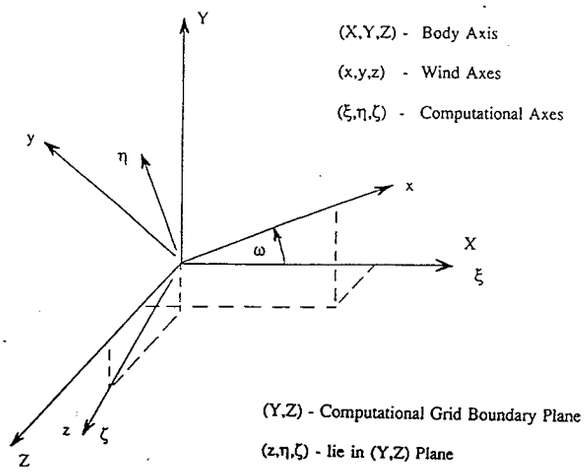

Fig. 3 Coordinate System Definition.

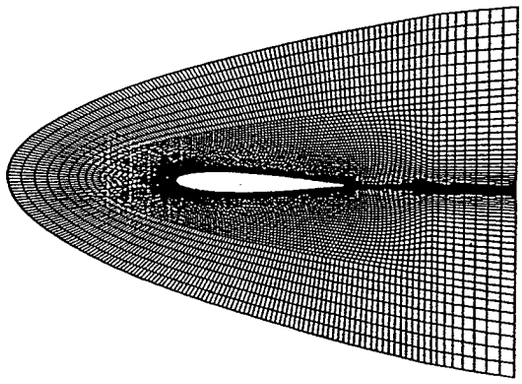

Fig. 4 Core Grid for NACA 0012 Airfoil.

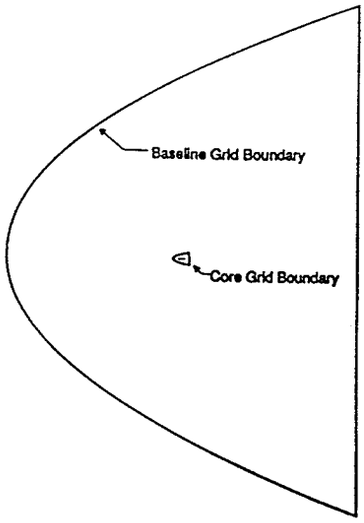

Fig. 5 Relative Boundary Locations of Baseline and Core Grids.

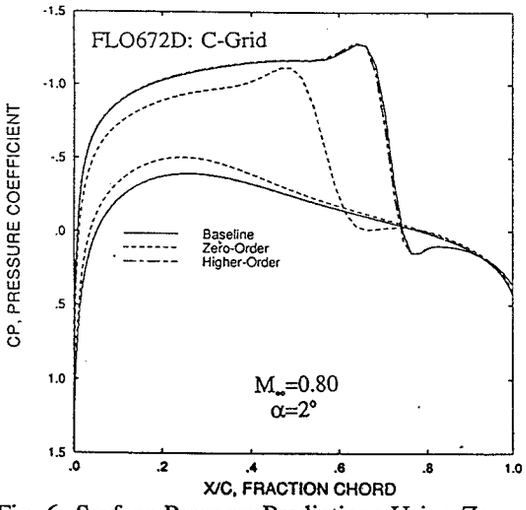

Fig. 6 Surface Pressure Predictions Using Zero- and Higher-Order Boundary Conditions.

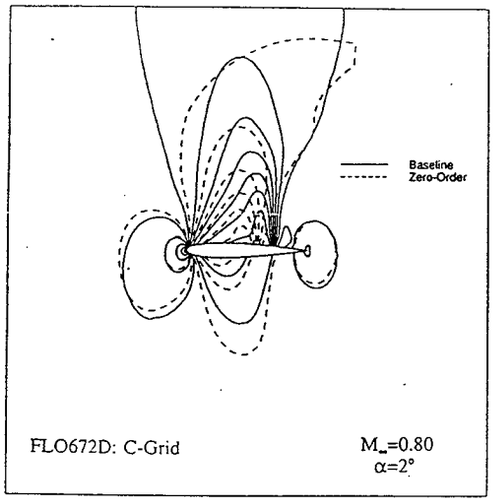

Fig. 7 Pressure Contours Predicted Using Zero-Order Boundary Conditions.

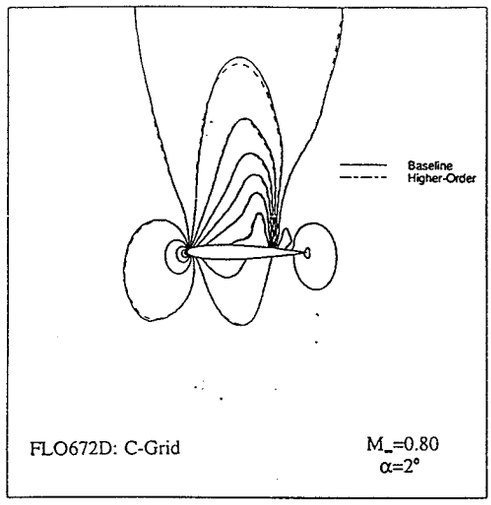

Fig. 8 Pressure Contours Predicted Using Higher-Order Boundary Conditions.

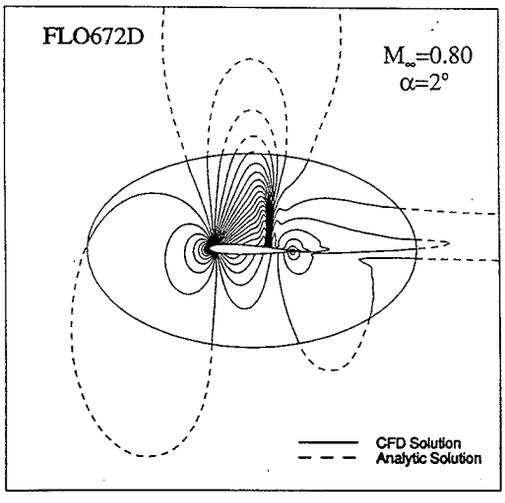

Fig. 9 Transonic Mach Number Contours With Far-Field Analytical Solution Added.

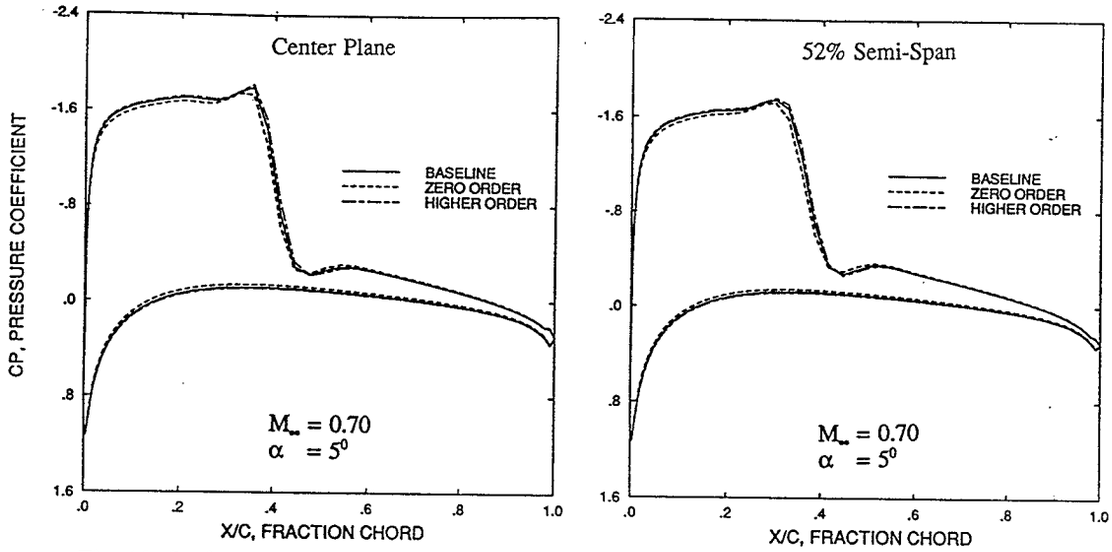

Fig. 10 Surface Pressure Predictions Using Zero- and Higher-Order Boundary Conditions.

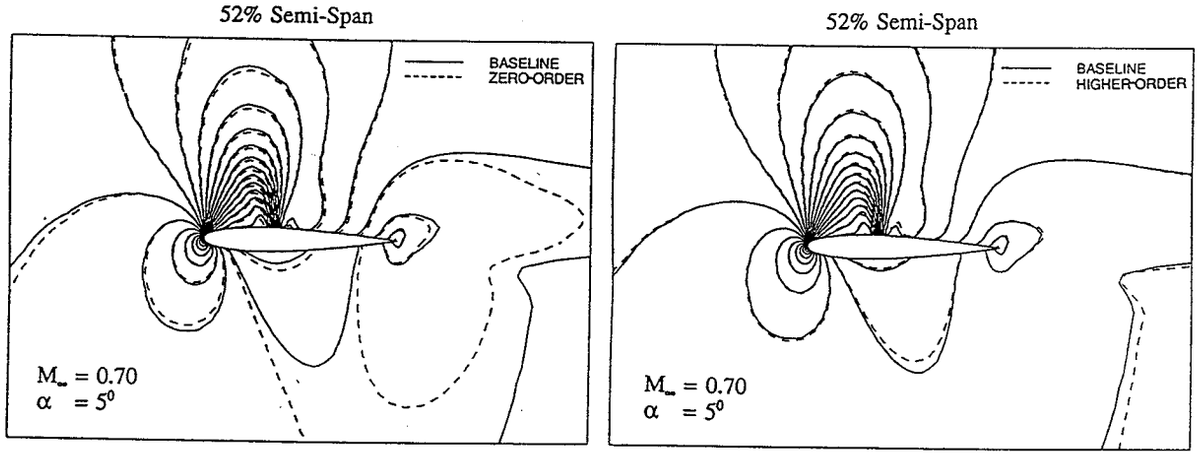

Fig. 11 Pressure Contours Predicted Using Zero- and Higher-Order Boundary Conditions.

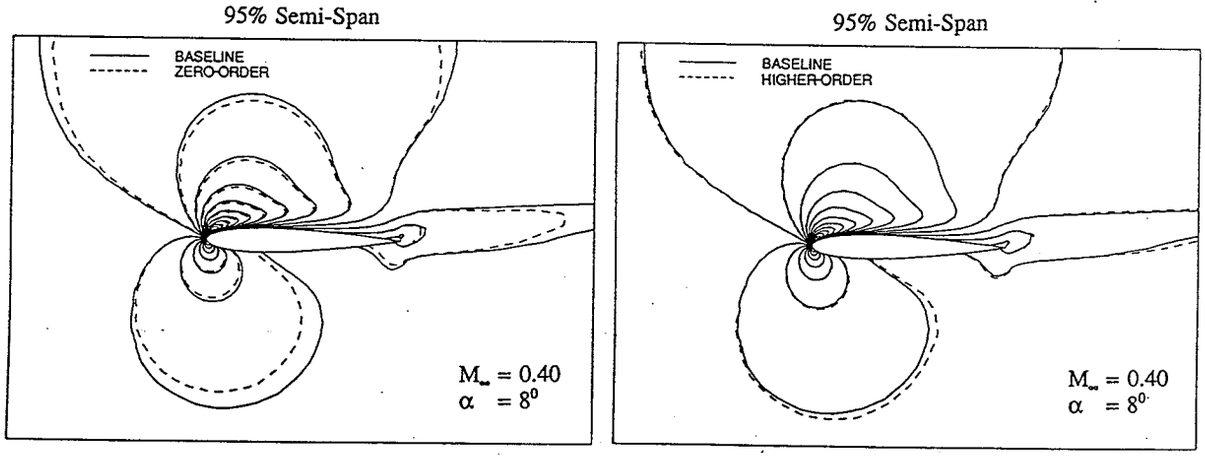

Fig. 12 Pressure Contours Predicted Using Zero- and Higher-Order Boundary Conditions.